Nanoscale

ROYAL SOCIETY OF CHEMISTRY

PAPER

View Article Online
View Journal

Check for updates

Cite this: DOI: 10.1039/d5nr04283f

An Mn^{2+}-coordinated glycyrrhizic acid self-adjuvating hydrogel for sustained codelivery of an antigen and Mn^{2+} for a potent immune response

Jingjing Zhou,[a] Shengying Zhang,[a] Hu Dong,[a] Yunhua Li,[b] Haoyue Zang,[a] Zhidong Teng,[a] Mingyang Zhang,[a] Yifan Liu,[a] Shiqi Sun*[a] and Huichen Guo *[a]

Received 10th October 2025,
Accepted 12th January 2026

DOI: 10.1039/d5nr04283f

rsc.li/nanoscale

The development of vaccine platforms that enable sustained codelivery of antigens and adjuvants remains a major challenge in modern vaccinology. Herein, we constructed a self-adjuvating hydrogel (GA@Mn) *via* the self-assembly of natural glycyrrhizic acid (GA) and subsequent coordination with Mn^{2+}. This coordination facilitates gradual Mn^{2+} release during hydrogel degradation, overcoming the rapid clearance and poor bioavailability of soluble Mn^{2+} *in vivo*. Notably, Mn^{2+} coordination drastically increased the cross-linking density of the GA hydrogel (GAgel) network, enhancing the storage modulus of GA@Mn by three orders of magnitude compared to the native GAgel. This superior mechanical stability allows GA@Mn to serve as an efficient antigen depot, prolonging the retention of both Mn^{2+} and the antigen at the injection site for up to 14 days. Meanwhile, GA@Mn promoted robust local immune cell recruitment, establishing an antigen-presenting cell (APC)-rich microenvironment. Subsequently, GA@Mn activation of the STING pathway enhanced the dendritic cell (DC) maturation and antigen uptake by 2.4-fold and 1.8-fold, respectively. In mice, a single injection of GA@Mn significantly potentiated antigen-specific humoral and cellular immune responses, leveraging a synergistic effect between the STING-activating capacity of Mn^{2+} and the depot-forming ability of the hydrogel. In summary, this study presents a facilely fabricated GA@Mn hydrogel vaccine platform that enables sustained codelivery of the antigen and adjuvant (Mn^{2+}) for robust immune enhancement. This work provides a new paradigm for the rational design of metal ion-coordinated hydrogel vaccines.

1. Introduction

Viruses cause a broad range of infectious diseases, which include conditions ranging from seasonal influenza to COVID-19, and often lead to considerable medical, economic, and social consequences. Vaccination remains the most effective strategy for preventing viral infections.[1] The protective efficacy of vaccines depends on adaptive immunity, which is synergistically initiated by antigens and adjuvants. By facilitating antigen depot formation, enabling targeted delivery, activating immune cells, and promoting antigen uptake, adjuvants play an essential role in modulating immune response profiles. These functions collectively contribute to enhanced vaccine potency, reduced antigen dosage, and lower production costs.[2,3] Despite their importance, adjuvant development has advanced slowly since the introduction of aluminum-based adjuvants (alum) in the 1920s, and it continues to lag far behind progress in antigen design. To date, only a limited number of adjuvants have been approved for clinical use.[4] Therefore, there is an urgent need for novel adjuvants that exhibit simple composition and clearly defined mechanisms.

Manganese (Mn^{2+}), which is an essential trace element, plays vital roles in the development, metabolism, and the maintenance of antioxidant homeostasis.[5] Notably, Jiang *et al.* revealed that Mn^{2+} potently activates the endoplasmic reticulum STING pathway, thereby triggering downstream signaling that stimulates the production of type I interferons (IFNs) and pro-inflammatory cytokines while also promoting the maturation of dendritic cells (DCs) and macrophages for enhanced antigen presentation.[6,7] These properties establish Mn^{2+} as a highly promising adjuvant candidate, particularly in its capacity to bolster Th1-mediated cellular immunity. However, free Mn^{2+} injected *in vivo* rapidly diffuses from the injection site into systemic circulation, where it is subject to swift metabolism and excretion, significantly limiting its immunostimulatory potential.[8] It is

---

[a] *State Key Laboratory of Animal Disease Control and Prevention, College of Veterinary Medicine, Lanzhou University, Lanzhou Veterinary Research Institute, Chinese Academy of Agricultural Sciences, Lanzhou, China.*
E-mail: sunshiqi@caas.cn, guohuichen@caas.cn

[b] *College of Chemistry and Chemical Engineering, Lanzhou University, Lanzhou, China*

therefore critical to incorporate Mn^{2+} into a delivery system that ensures sustained release in order to maximize its adjuvant efficacy, which represents a major hurdle for the clinical translation of metal ion-based adjuvants.

Self-assembly of free drugs into nanomedicines represents a promising strategy for achieving controlled delivery.[9] While various materials, such as nanoparticles, electrospun fibers, emulsions, and hydrogels, have been employed for antigen and adjuvant delivery,[10,11] many conventional systems often lack the structural features needed for efficient signaling interactions with surrounding cells or tissues.[12] Hydrogels possess a porous, nanofibrous architecture that mimics the extracellular matrix, serving as scaffolds that support cell migration, immune cell recruitment, and localized antigen processing and presentation.[13–15] Their solid-like nature allows the formation of persistent depots at the injection site, which may enhance Th2-biased humoral immunity.[16] Among them, hydrogels formed through direct self-assembly of natural small molecules have attracted interest due to their simple preparation and favorable biocompatibility.[17,18] These carrier-free systems eliminate the need for exogenous crosslinkers and allow gentle antigen incorporation *via* mixing, holding significant potential for vaccine applications.[19] Glycyrrhizic acid (GA), a natural amphiphile derived from traditional Chinese medicine, consists of a hydrophobic triterpenoid aglycone (18β-glycyrrhetinic acid) and a hydrophilic D-glucuronic acid unit, enabling its self-assembly in an aqueous solution into low-molecular-weight hydrogels.[20–22] However, almost all hydrogel platforms are unable to achieve the sustained co-delivery of antigens and adjuvants, which is crucial for inducing a potent immune response. Metal ion coordination provides a robust alternative for engineering hydrogel systems, where the coordinated ions not only facilitate molecular assembly but also serve as inherent immune adjuvants.[23,24] Inspired by this approach, we developed a coordination-mediated coassembly strategy between GA and Mn^{2+}. As illustrated in Scheme 1, Mn^{2+} coordination facilitated the formation of a reinforced hydrogel designated GA@Mn. Then, we systematically investigated its formation mechanism, rheological properties, and sustained release profile for both the antigen and Mn^{2+}. In our previous work, we successfully prepared foot-and-mouth disease virus-like particles (FMD VLPs) with an average diameter of 25 nm using an *E. coli* expression system. These VLPs elicited robust protective immune

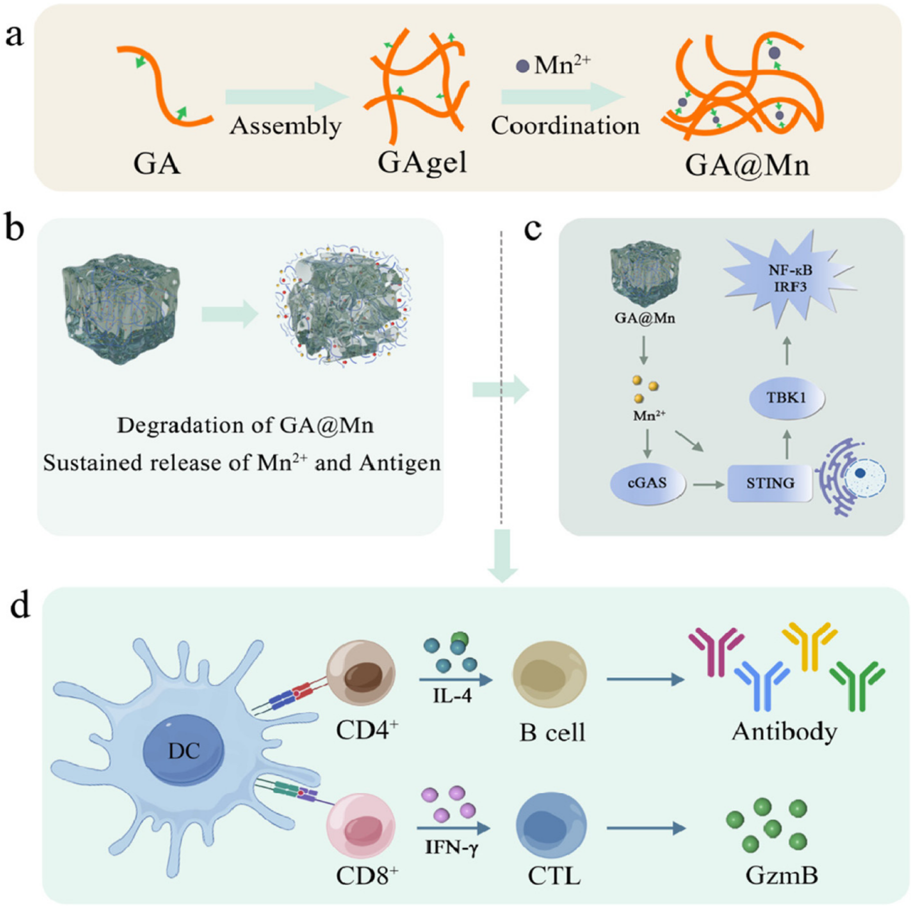

Scheme 1 Schematic of GA@Mn hydrogel preparation and biological function. (a) Mn^{2+} coordination-driven GA@Mn hydrogel formation. (b) Gradual degradation of GA@Mn with sustained Mn^{2+} and antigen release. (c) The STING pathway was activated by released Mn^{2+}. (d) GA@Mn vaccine platform eliciting robust humoral and cellular immunity.

responses in guinea pigs, pigs, and cattle.[25] Here, we loaded FMD VLPs into the GA@Mn hydrogel and comprehensively evaluated its ability to activate innate immunity, recruit and mature immune cells, and elicit antigen-specific humoral and cellular immune responses.

2. Experimental

2.1. Materials

Manganese chloride tetrahydrate ($MnCl_2 \cdot 4H_2O$) was purchased from Shanghai Macklin Biochemical Co., Ltd (China). GA ($C_{42}H_{62}O_{16}$) was purchased from Beijing Solarbio Science & Technology Co., Ltd (China). Dulbecco's Modified Eagle's Medium (DMEM) and fetal bovine serum (FBS) were obtained from Gibco (USA). 3-(4,5-Dimethylthiazol-2-yl)-5-(3-carboxymethoxyphenyl)-2-(4-sulfophenyl)-2*H*-tetrazolium inner salt (MTS) was purchased from Promega (China). The calcein-AM/PI double stain kit was purchased from Solarbio (China). The pre-coated mouse IFN-γ ELISpot kit was purchased from Dakewei (China) and the mouse GzmB ELISA kit was purchased from Mlbio (China). Mouse OVA-IgG, OVA-IgG1, and OVA-IgG2a ELISA kits were purchased from Mlbio (Shanghai, China).

2.2. Animals

Female BALB/c mice (6–8 weeks old, weighing 18–22 g) were obtained from the Laboratory Animal Center of the Lanzhou Veterinary Research Institute, Chinese Academy of Agricultural Sciences. The mice were housed under standard temperature-controlled conditions with *ad libitum* access to food and water. The minimum number of animals necessary was used, and all efforts were made to minimize distress. Following experimental procedures, animals were euthanized. All the experiments in this study were carried out under the European Communities Council Directive of 24 November 1986 (86/609/EEC) and approved by the Animal Management and Ethics Committee of the Lanzhou Veterinary Research Institute, Chinese Academy of Agricultural Sciences (Approval No. LVRIAEC-2024-027).

2.3. Hydrogel formation

Aqueous solutions of $MnCl_2$ or $AlCl_3$ at different concentrations (0, 0.5 mM, 1 mM, 2.5 mM, and 5 mM) were added to the GA solution, respectively. The mixtures were cooled to room temperature to obtain GA@Mn or GA@Al hydrogels. The final concentration of GA was 3% (w/v).

2.4. Scanning electron microscopy (SEM)

The hydrogel microstructure and Mn^{2+} distribution were characterized using an Apreo S SEM (Thermo Fisher Scientific, USA). Samples were deposited onto silicon wafers and air-dried at room temperature, and then sputter-coated with a thin gold layer. SEM imaging and energy-dispersive X-ray spectroscopy (EDS) mapping were performed.

2.5. Isothermal titration calorimetry (ITC)

Mn^{2+} binding to GA was measured using a MicroCal PEAQ-ITC instrument (Malvern Instruments, UK). A total of 40 μL of $MnCl_2$ solution (5 mM) was titrated into 280 μL of GA solution (250 μM) at 25 °C with stirring at 1500 rpm. The protocol consisted of 13 automated injections: an initial 0.4 μL injection followed by 12 injections of 3 μL each, at 150 s intervals. The heat flow was recorded over time, and thermodynamic parameters including dissociation constant (K_D), binding stoichiometry (n), and enthalpy change (ΔH) were calculated using the instrument's software.

2.6. Fourier transform infrared (FTIR) analysis

FTIR spectroscopy was performed on the GAgel and GA@Mn hydrogels using an FTIR spectrometer (TENSOR 27, Bruker, Germany). Their freeze-dried powders were separately mixed with potassium bromide (KBr) and pressed into pellets. The infrared spectra were then recorded in the wavenumber range of 500–4000 cm^{-1}.

2.7. Rheological analysis

Rheological properties were determined using a HAAKE RS6000 rheometer (Thermo Fisher Scientific, USA) with a 35 mm parallel plate geometry at 25 °C. Tests included: (1) strain sweep (0.1–100% strain) to define the linear viscoelastic region (LVR); (2) frequency sweep (0.1–100 rad s^{-1}) at 1% strain; (3) time sweep at 1% strain and 1 Hz for 900 s; and (4) step–strain injectability tests, three cycles of 5 min at 1% strain followed by 1 min at 100% strain, recording the storage modulus (G') and loss modulus (G'').

2.8. Storage stability of the GA@Mn hydrogel

200 μL of the prepared GA@Mn hydrogel was placed in a 15 mL centrifuge tube. The samples were stored at room temperature for 5 days, 10 days, and 10 months, respectively. Then, photographs were taken to record the hydrogel integrity. SEM and EDS imaging analyses were performed as described in Section 2.4. Finally, time sweep and step–strain tests were carried out as described in Section 2.6 to evaluate the mechanical properties of the hydrogels.

2.9. MTS cytotoxicity assay

The cytotoxicity of the FMD VLPs, GAgel and GA@Mn hydrogels was assessed using Vero, DC2.4, and BHK cell lines. Hydrogel leachates were prepared by incubating the hydrogels in 1 mL of DMEM at 37 °C for 24 h. The cells were seeded 1 × 10^6 cells per well in 96-well plates and incubated for 24 h before replacing the medium with leachates or control DMEM. After an additional 24 h, 10 μL of MTS reagent was added and incubated for 2 h. Absorbance at 490 nm was measured (Synergy multi-mode microplate reader, BioTek, USA) and cell viability (%) was calculated as: cell viability (%) = $[OD_{sample}/OD_{control}] \times 100$.

2.10. Calcein-AM/PI cytotoxicity assay

Cells were co-cultured with hydrogel leachates in 24-well plates for 24 h, and then stained using the calcein-AM/PI kit per the manufacturer's instructions. The morphology and density were observed using a TH4-200 fluorescence microscope (Olympus, Japan).

2.11. *In vitro* degradation of hydrogels

The *in vitro* degradation profiles of the GAgel and GA@Mn hydrogels were investigated gravimetrically. The hydrogels loaded with FITC-OVA were immersed in 400 μL of PBS (0.01 M, pH 7.4), overlaid with an additional 400 μL PBS, and incubated under simulated physiological conditions (37 °C, 60% relative humidity). At 24 h intervals, the supernatant PBS was collected, the residual hydrogel mass was recorded, and fresh PBS of equal volume was added. This cycle was repeated until complete degradation. Degradation behavior was quantified by calculating hydrogel mass retention over time.

2.12. *In vitro* antigen release

The release kinetics of FITC-OVA from the GAgel and GA@Mn hydrogels were monitored using fluorescence spectroscopy. The supernatant samples were analyzed at an excitation wavelength of 490 nm and an emission wavelength of 525 nm using an FLS 1000 spectrofluorometer (Edinburgh Instruments, UK). Cumulative antigen release was calculated from fluorescence measurements to generate release profiles.

2.13. *In vitro* Mn^{2+} release

Mn^{2+} release from GA@Mn was quantified by inductively coupled plasma mass spectrometry (ICP-MS). Mn^{2+} concentrations in the collected supernatants were measured to determine temporal release profiles.

2.14. *In vivo* antigen and Mn^{2+} biodistribution

BALB/c mice were subcutaneously injected with 200 μL of $Mncl_2$ containing Cy5-OVA, the GAgel loaded with Cy5-OVA, or GA@Mn loaded with Cy5-OVA. At predetermined time points (1, 3, 7, 10, 14, and 21 days post-injection), the mice were anesthetized with isoflurane and imaged using an AniView 100 *in vivo* imaging system (Biolight Biotechnology Co., Ltd, China). Antigen biodistribution was evaluated from Cy5 fluorescence signals. Tissues from the injection site and the major organs (heart, liver, lungs, spleen, and kidneys) were collected at each time point, and the Mn^{2+} content was quantified by ICP-MS. At 0, 0.5, 1, 3, 5, and 10 days post-injection, peripheral blood was collected from the injected mice, and the Mn^{2+} content in the blood was determined by ICP-MS. On days 5 and 10 post-injection, peripheral blood was collected separately from the injected mice for blood biochemical tests. The tested indicators included albumin (ALB), alanine aminotransferase (ALT), aspartate aminotransferase (AST), creatinine (CREA), uric acid (UA), and urea nitrogen (UREA).

2.15. The expression of STING pathway-related proteins

Western blotting (WB) was employed to analyze the expression levels of proteins associated with the STING signaling pathway. DC2.4 cells were seeded 5 × 10^5 cells per well in 6-well plates and treated with GAgel leachate, $MnCl_2$ solution, or GA@Mn leachate; blank medium served as the control. After 12 h, the cells were lysed in 1 × SDS denaturing buffer and heat-denatured. Proteins were separated by SDS-PAGE and transferred to PVDF membranes by wet transfer. The membranes were blocked and probed with primary antibodies against phosphor-STING (p-STING), phospho-IRF3 (p-IRF3), phospho-TBK1 (p-TBK1), and β-tubulin. After overnight incubation at 4 °C, the membranes were treated with HRP-conjugated goat anti-rabbit secondary antibody for 1 h at room temperature. Bands were visualized by ECL chemiluminescence (Tanon, Shanghai).

2.16. The mRNA expression of cGAS-STING pathway-related cytokines

The mice were subcutaneously injected with 200 μL of PBS, FMD VLPs, $MnCl_2$, the GAgel, or GA@Mn, respectively. At 24 h post-injection, injection site tissue was collected, homogenized in Trizol, and processed for RNA extraction. cDNA synthesis and RT-PCR were performed according to the classical methods. GAPDH served as the reference, and the relative expression of cGAS-STING pathway-related cytokines was calculated using the $2^{-\Delta\Delta CT}$ method. Primer sequences are provided in Table S1.

2.17. DC activation

The activation of DCs was evaluated *via* flow cytometry, focusing on the expression of surface co-stimulatory molecules. BMDCs were seeded 5 × 10^5 cells per well in 12-well plates and incubated for 12 h before treatment with $MnCl_2$ solution, GAgel leachate, or GA@Mn leachate. The medium alone served as the negative control and the medium containing lipopolysaccharide (LPS, 10 μg mL^{-1}) served as the positive control. After 24 h, the cells were stained with anti-mouse CD11c-PerCP-Cy5.5, CD80-BV421, and CD86-PE-Cy7 antibodies. The samples were analyzed using a CytoFLEX LX flow cytometer (Beckman Coulter, USA), and the expression of CD80 and CD86 on $CD11c^+$ cells was quantified.

2.18. Antigen uptake

Antigen uptake was evaluated using confocal laser scanning microscopy (CLSM). BMDCs were seeded 5 × 10^5 cells per well onto glass coverslips and allowed to adhere. The medium alone served as the negative control. The cells were treated with $Mncl_2$, the GAgel, and GA@Mn leachate containing 20 μL of OVA-FITC. After 12 h of incubation, the cells were fixed with 4% paraformaldehyde for 15 min, stained with DAPI for 15 min at room temperature, and mounted for imaging. Fluorescence distribution of the FITC-labeled antigen was visualized using CLSM (Zeiss LSM 980 with Airyscan 2, Germany), and antigen uptake was quantified based on fluorescence intensity.

2.19. Immune cell recruitment

Immune cell recruitment to the hydrogel injection site was assessed by histology and flow cytometry. The mice received subcutaneous injections (200 μL) of the hydrogel. On day 5 post-injection, the nodule at the injection site was excised; one portion was fixed in 4% paraformaldehyde, paraffin-embedded, sectioned, and stained with hematoxylin and eosin (H&E) for histological assessment. Paraffin sections were incubated with antibodies corresponding to CD11c, CD11b, Ly-6G, and CD49b for 12 h. After removing unbound antibodies, the sections were incubated with Cy3-conjugated goat anti-rabbit IgG and DAPI, respectively. Finally, the distribution of immune cells was observed and recorded using a confocal laser scanning microscope.

The remaining tissue was mechanically dissociated and digested for 3 h at 37 °C in 10 mL of Hank's solution to prepare a single-cell suspension, which was counted and adjusted to 1×10^7 cells per millilitre. A 100 μL aliquot was stained with antibodies against mouse CD11c-PerCP-Cy5.5, CD11b-PE-CF594, F4/80-PE, CD49b-APC, and Ly-6G-BV650. The stained cells were analyzed by flow cytometry to determine the proportions of DCs (CD11c$^+$), macrophages (CD11b$^+$F4/80$^+$), NK cells (CD49b$^+$), and neutrophils (Ly-6G$^+$).

2.20. Specific antibody and neutralizing antibody assays

Foot-and-mouth disease virus-like particles (FMD VLPs) were employed as the antigen to prepare GAgel and GA@Mn hydrogel vaccines. Solution-based vaccines were formulated by dispersing FMD VLPs in PBS or $MnCl_2$ solution. PBS was used as the control. The mice received a single immunization with an FMD VLP dose of 10 μg per mouse. Serum antibody levels were measured using a liquid-phase blocking ELISA kit for FMD. 96 well plates were coated with 100 μL per well of diluted FMDV-specific primary antibody and incubated overnight at 4 °C. Diluted serum samples pre-mixed with FMD VLPs were then added (100 μL per well) and incubated at 37 °C for 30 min, followed by addition of IgG-HRP-conjugated secondary antibody (100 μL per well) for 30 min. Color development was achieved with a TMB substrate (100 μL per well) for 15 min, and the reaction was stopped with 50 μL per well of 2 M H_2SO_4. Absorbance at 450 nm was recorded using a Synergy H1 multimode microplate reader. Using a liquid-phase blocking ELISA established with the single-domain antibody M8 and O-type FMD VLPs, the levels of neutralizing antibodies were assessed. In 96-well plates, 100 μL of diluted antibody M8 was added to each well and incubated overnight at 4 °C. Subsequently, the diluted serum samples pre-mixed with the O-type VLP antigen were added to the plates and incubated at room temperature for 1 h. Next, labeled M652 antibody was added and incubated at room temperature for 1 h. This was followed by the addition of HRP-conjugated secondary antibody and incubated at room temperature for 1 h. Finally, the TMB substrate was added for color development, and the absorbance at 450 nm was measured using a microplate reader.

2.21. IgG1 and IgG2a subtypes

IgG1 and IgG2a levels in mouse serum were determined by indirect ELISA. Plates were coated overnight at 4 °C with 1 μg per well of FMD VLPs, and then blocked with 5% skim milk for 1 h. The diluted serum samples (100 μL per well) were added and incubated at 37 °C for 1 h, followed by HRP-conjugated goat anti-mouse IgG1 or IgG2a antibodies for 1 h. The TMB substrate (100 μL per well) was added for 15 min and the reaction was stopped with 50 μL per well of 2 M H_2SO_4. Absorbance at 450 nm was measured using a Synergy H1 multimode microplate reader.

2.22. OVA-specific antibodies and their subtypes

To evaluate the antigen generality of the vaccine platform, immunization was performed using the model antigen ovalbumin (OVA). The OVA antigen was loaded into the GAgel and GA@Mn hydrogels to prepare OVA–GAgel and OVA–GA@Mn vaccines, respectively. Control vaccines were prepared by dispersing OVA in PBS or $MnCl_2$ solution. The mice received a single immunization with an OVA dose of 10 μg per mouse. Serum was collected on day 28 post-immunization. Commercial mouse anti-OVA IgG, IgG1, and IgG2a ELISA kits were used to determine the levels of OVA-specific antibodies and antibody subtypes in the serum on day 28.

2.23. The mRNA expression levels of GC B-related cytokines

Lymph nodes were harvested from the mice and homogenized using Trizol reagent for RNA extraction. cDNA was synthesized following established protocols. The relative mRNA expression levels of GC B-associated factors Bcl-6 and Bach2 were quantified *via* RT-PCR. GAPDH served as the reference gene, and the relative expression levels were calculated using the $2^{-\Delta\Delta CT}$ method. Primer sequences are provided in Table S2.

2.24. Isolation of lymphocytes

The lymph node or spleen was aseptically removed, mechanically dissociated, and passed through a 200-mesh nylon screen. Single-cell suspensions were prepared using a murine lymphocyte density gradient separation kit (Dakewe, Beijing). After centrifugation at 800*g* for 30 min, the lymphocyte layer was collected, washed with 10 mL of RPMI 1640 medium, and centrifuged at 400*g* for 5 min at 4 °C. The final cell suspension was adjusted to 1×10^7 cells per millilitre for further assays.

2.25. IL-4 and IFN-γ secretion

The frequencies of IL-4- and IFN-γ-secreting splenic lymphocytes were determined using a mouse IL-4/IFN-γ precoated ELISpot kit. PVDF membrane plates were equilibrated with 200 μL per well of RPMI 1640 medium before seeding 1×10^6 per well cells of lymphocyte suspension. The cells were incubated for 18 h, followed by washing, conjugate addition, and substrate development according to the manufacturer's protocol. Spots representing the cytokine-secreting cells were visualized and counted using an IRIS ASTOR ELISpot reader (Mabtech, Sweden).

2.26. GzmB secretion

Granzyme B (GzmB) secretion by splenic lymphocytes from the immunized mice was quantified using a mouse GzmB ELISA kit. Splenic lymphocyte suspensions were seeded at 1 × 10^5 per well cells in 96-well culture plates and stimulated with 2 μg of antigen for 18 h. After stimulation, the supernatants were collected by centrifugation at 1000*g* for 15 min at 4 °C. Aliquots were transferred to GzmB antibody-precoated plates, and subsequent assay steps were performed according to the manufacturer's instructions. Absorbance at 450 nm was measured using a microplate reader, and GzmB concentrations were calculated from the standard curve.

2.27. GC B, TCM, and TEM cells

Lymphocytes were adjusted to 1 × 10^6 per well cells and analyzed by flow cytometry. The proportions of GC B cells ($B220^+CD95^+GL7^+$), central memory T cells (TCM, $CD44^+CD62L^+$), and central effector memory T cells (TEM, $CD44^+CD62L^-$) were determined.

2.28. *In vivo* biocompatibility

Hydrogel biocompatibility was assessed 56 days post-immunization by histopathological and hematological analyses. The mice were euthanized and the major organs (heart, liver, spleen, kidneys, and lung) were collected for H&E staining. Whole blood was analyzed for hematological parameters, including hemoglobin (HGB), mean corpuscular hemoglobin (MCH), the mean corpuscular hemoglobin concentration (MCHC), the mean corpuscular volume (MCV), the red blood cell (RBC) count, and the white blood cell (WBC) count. Serum was analyzed for biochemical indicators, including ALB, ALT, AST, CREA, UA, and UREA.

3. Results and discussion

3.1. Mn^{2+} coordinates with the natural small molecule GA to form the GA@Mn hydrogel

Previous studies have demonstrated that the natural small molecule GA (Fig. 1a) can self-assemble into nanofibers and form a hydrogel GAgel (Fig. S1).[26–28] In this work, we investigated the coordination-driven assembly between GA and Mn^{2+} (Fig. 1b). The vial inversion results showed that the addition of Mn^{2+} significantly promoted hydrogel formation. The stability of the GA@Mn hydrogel gradually increased with higher Mn^{2+} concentrations (Fig. 1c and Fig. S2). Considering the important influence of the hydrogel's mechanical properties on its function as an antigen depot, we selected the GA@Mn hydrogel formed with 5 mM Mn^{2+} for subsequent studies. The SEM images revealed that GA@Mn consists of abundant supramolecular nanofibers organized into a densely crosslinked network (Fig. 1d). Unbound Mn^{2+} was subsequently removed *via* three cycles of centrifugation (1500*g*, 5 min), yielding purified GA@Mn nanofibers. EDS mapping confirmed the homogeneous distribution of Mn^{2+} throughout the nanofibers, alongside carbon (C), indicating stable coordination between Mn^{2+} and GA (Fig. 1e). ITC was further employed to quantify the Mn^{2+}–GA interaction. Titration of Mn^{2+} into the GA solution produced an endothermic binding isotherm (Fig. 1f). Fitting the data to a one-site binding model (Fig. 1g) yielded an N of 0.15, a K_D of 2.27 × 10^{-3} M, and a ΔH of −2.17 kcal mol^{-1}, confirming and quantitatively characterizing the coordination interaction between GA and Mn^{2+}. Furthermore, FTIR analysis was conducted to investigate the interaction between GA and Mn^{2+}. The results (Fig. S3) showed that, compared to the GAgel, the C=C stretching band in GA@Mn shifted to lower wavenumbers. Furthermore, the intensities of the O–H stretching band, the $-CH_3$ stretching band, and the C–O stretching band were reduced, indicating a strong binding interaction between GA and Mn^{2+}.[29,30]

Considering the widespread use of aluminum ions (Al^{3+}) in vaccine adjuvants, we also investigated the assembly between GA and Al^{3+}. Titration of Al^{3+} into the GA solution produced a distinct exothermic binding isotherm (Fig. S4). The SEM images revealed that GA@Al also consists of a supramolecular nanofiber network (Fig. S5). EDS mapping similarly confirmed the homogeneous distribution of Al^{3+} alongside carbon (C) throughout the nanofibers, indicating a stable coordination between Al^{3+} and GA (Fig. S5). Finally, we examined the potential of Al^{3+} and GA to co-assemble into a hydrogel using different Al^{3+} concentrations. The vial inversion results (Fig. S6) indicated that a stable hydrogel forms when the Al^{3+} concentration reaches 1 mM. However, when the concentration increases to 5 mM, GA@Al exhibits some fluidity, suggesting that a higher dose of Al^{3+} is not conducive to forming a stable GA@Al hydrogel. These results demonstrate that Al^{3+} can coordinate with GA and form a stable hydrogel at appropriate concentrations. Unlike Al^{3+}, Mn^{2+} can activate the STING pathway and promote a Th1-biased immune response. Therefore, in subsequent studies, we focused primarily on investigating the biological functions of GA@Mn.

3.2. Mn^{2+} coordination significantly enhances the mechanical properties of GA@Mn

The mechanical properties of hydrogel-based vaccine delivery systems are critical for both injectability and antigen depot formation.[31] Here, the strength of the hydrogel was characterized *via* rheological measurements. The GAgel exhibited a broad LVR, with the G' and G'' intersecting at strains above 40%, after which G' dropped below G'', indicating a transition from the hydrogel to sol state (Fig. 1h). In contrast, GA@Mn displayed a narrower LVR, transitioning at strains above 10%. Frequency and time sweep tests showed that the G' of GA@Mn was nearly three orders of magnitude higher than that of the GAgel, with both G' and G'' remaining stable throughout testing (Fig. 1i and j), demonstrating significantly enhanced mechanical strength, stability, and viscoelasticity. Creep-recovery tests under high strain (100%) followed by low strain (1%) showed that both the hydrogels exhibited $G'' > G'$ under high

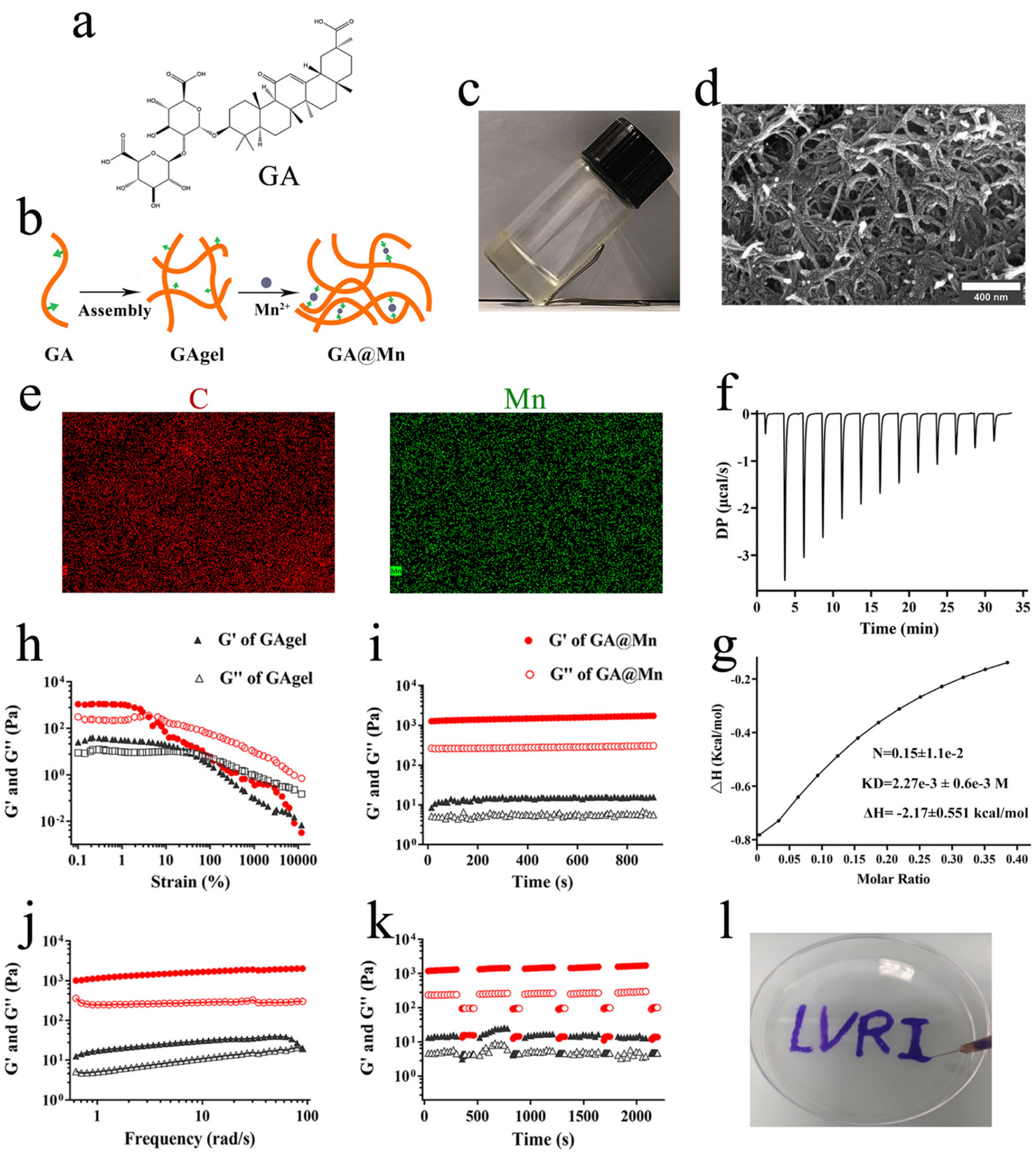

Fig. 1 Preparation and characterization of GA@Mn. (a) The chemical structure of GA. (b) Schematic illustration of GA@Mn preparation. (c) Optical image of GA@Mn. (d) SEM image of the GA@Mn microstructure. (e) EDS elemental mapping of C or Mn in the GA@Mn nanofibers. (f and g) Mn^{2+} titration curves with GA and thermodynamic parameters. (h) Strain sweep of the GAgel and GA@Mn at 1 Hz. (i) Time sweep of the GAgel and GA@Mn at 1% strain and 1 Hz. (j) Frequency sweep of the GAgel and GA@Mn at 1% strain. (k) Step–strain test: alternating 1% strain (300 s) and 100% strain (60 s) for five cycles. (l) Photograph of "LVRI"-extruded GA@Mn through a syringe needle.

strain, reflecting the loss of elastic behavior (Fig. 1k). Upon return to low strain, each hydrogel rapidly recovered its original mechanical properties, indicating efficient self-healing capability (Fig. 1k). This feature enables GA@Mn to promptly form a stable antigen depot at the injection site. Injectability was further confirmed by extruding the GA@Mn through a 0.45 mm syringe needle, which produced continuous strands without rupture (Fig. 1l), confirming its suitability for injection.

3.3. The GA@Mn hydrogel exhibits excellent storage stability

The storage stability of a vaccine platform is crucial for its practical application. To further evaluate the application potential of GA@Mn, the hydrogel was stored at room temp-

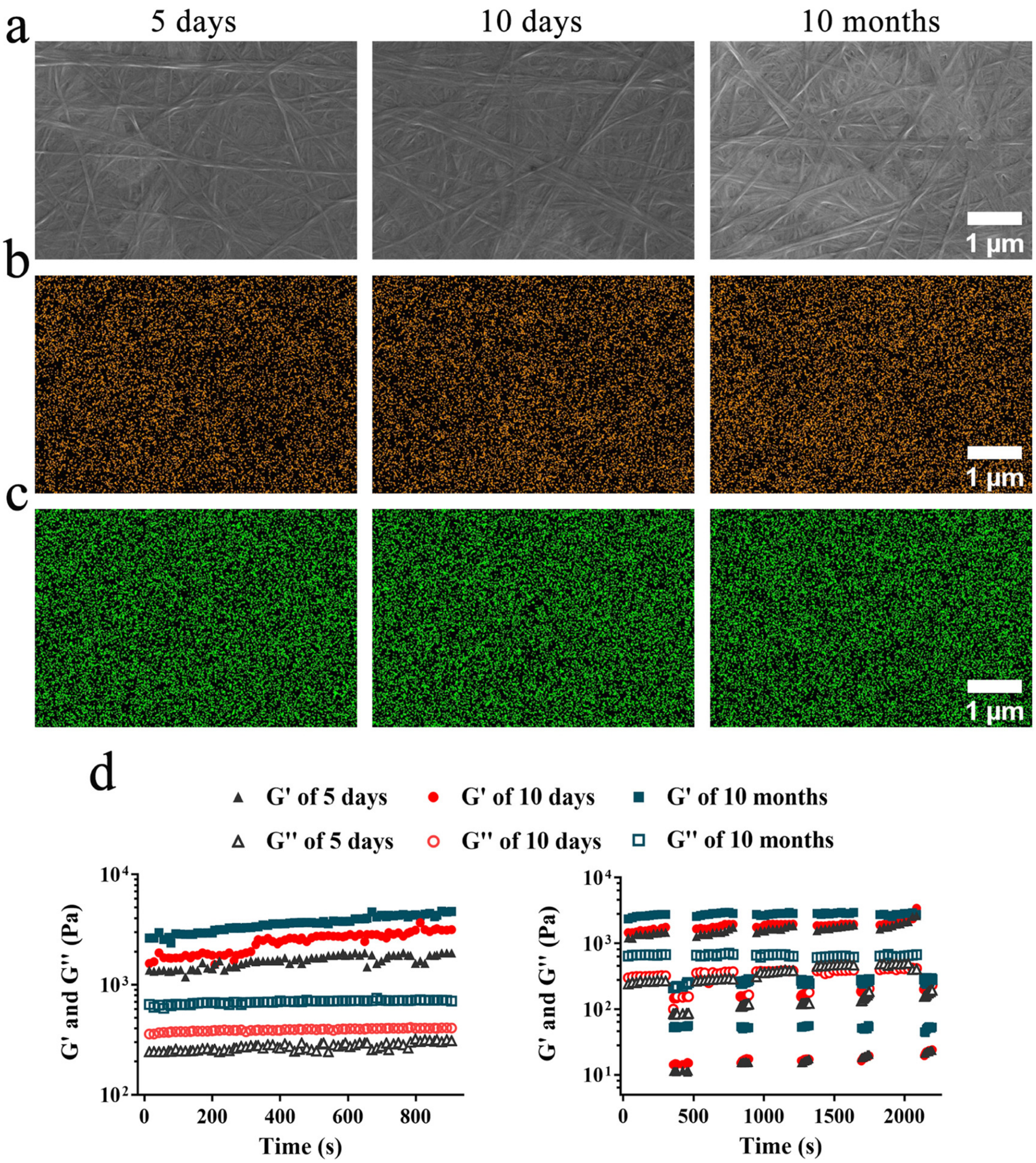

Fig. 2 Storage stability of the GA@Mn hydrogel. (a) SEM images of the microstructure of GA@Mn after storage at room temperature for 5 days, 10 days, and 10 months. (b and c) EDS elemental mapping showing the distribution of carbon (b) and manganese (c) in the nanofibers of GA@Mn after storage at room temperature for 5 days, 10 days, and 10 months. (d) Time sweep and step–strain tests performed on GA@Mn after storage at room temperature for 5 days, 10 days, and 10 months.

erature for 5 days, 10 days, and 10 months to assess its stability. The photographic results (Fig. S7) indicated that the GA@Mn hydrogel maintained good integrity even after 10 months of storage at room temperature. Furthermore, we observed the microstructure of GA@Mn after different storage periods using SEM. The SEM results (Fig. 2a) revealed that the GA@Mn hydrogel retained a network structure composed of stable supramolecular nanofibers even after 10 months of storage at room temperature. EDS mapping (Fig. 2b and c) showed a homogeneous distribution of Mn^{2+} and carbon (C) elements throughout the nanofibers, indicating that the stable coordination between Mn^{2+} and GA persisted. Time sweep tests (Fig. 2d) demonstrated that the G' values of GA@Mn remained significantly higher than the G'' values and were stable throughout the testing period after storage for 5 days, 10 days, and 10 months. In step–strain tests (Fig. 2d), all tested samples exhibited the characteristic $G'' > G'$ under high strain and rapidly recovered their original mechanical properties upon returning to low strain. This indicates that the GA@Mn hydrogel maintained excellent injectability after 5 days, 10 days, and even 10 months of storage at room temperature. Notably, in both testing modes, the G' values of the hydrogel

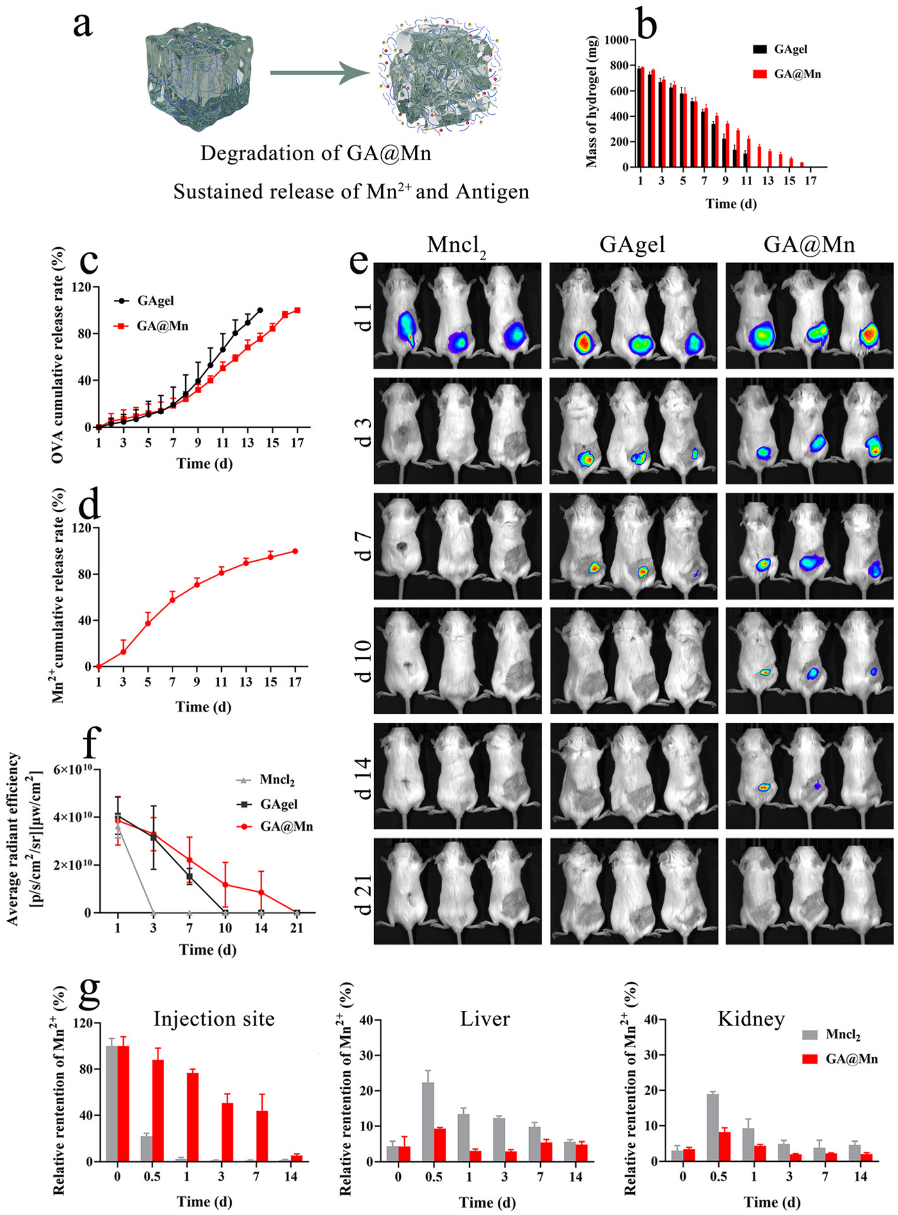

Fig. 3 GA@Mn sustained release of the antigen and Mn^{2+} *via* gradual degradation *in vitro* and *in vivo*. (a) Schematic illustration of GA@Mn degradation and release profile of the antigen and Mn^{2+}. (b) *In vitro* degradation of the GAgel and GA@Mn. (c) *In vitro* antigen release kinetics. (d) *In vitro* Mn^{2+} release kinetics from GA@Mn. (e) *In vivo* fluorescence images of the mice injected with $MnCl_2$, the GAgel, and GA@Mn containing FITC-OVA. (f) Quantification of fluorescence intensity at the injection site. (g) Mn^{2+} content at the injection site, liver, and kidneys.

stored for 10 months were higher than those stored for 5 or 10 days. This may be attributed to the formation of more stable cross-links within the nanofiber network over time.

3.4. Excellent cytocompatibility of the GA@Mn hydrogel

Biocompatibility is a fundamental requirement for hydrogel-based biomedical applications. To assess the cytocompatibility of GA@Mn, we incubated its leach solutions with BHK, DC2.4, and Vero cells for 24 h. Cell viability was evaluated using the MTS assay, while live/dead staining was employed to examine morphological integrity. All treatment groups showed cell viability exceeding 95%, with no significant differences observed between groups (Fig. S8a), indicating that neither the GAgel nor GA@Mn adversely affected cell proliferation. The live/dead staining images revealed intact cellular structures and normal morphology across all groups, comparable to the control (Fig. S8b). These results demonstrate the excellent cytocompatibility of GA@Mn and support its potential for further *in vivo* applications.

3.5. GA@Mn enables sustained release of the antigen and Mn^{2+}

Prolonged antigen release enhances immune responses by improving antigen bioavailability, extending interactions with immune cells, and promoting persistent GC activation.[32] In this study, we first evaluated the *in vitro* degradation profiles of the GAgel and GA@Mn, along with their respective antigen and Mn^{2+} release behaviors (Fig. 3a). The hydrogels were incubated in PBS, with supernatants collected every 24 h to measure the remaining mass, antigen concentration, and Mn^{2+} content. The GAgel degraded completely within 12 days, while GA@Mn required 17 days (Fig. 3b). Antigen release correlated closely with matrix degradation: the GAgel released its entire antigen payload by day 12, whereas GA@Mn completed release on day 17 (Fig. 3c). This synchronized release suggests that both hydrogels restrict rapid antigen leakage *via* their nanofiber networks, with GA@Mn's enhanced mechanical strength contributing to its more sustained profile. Similarly, Mn^{2+} release from GA@Mn was completed over 17 days (Fig. 3d). In contrast to free ions, which often leak rapidly, the coordination between Mn^{2+} and GA enables a gradual release aligned with hydrogel disintegration. We next investigated antigen biodistribution *in vivo* using live imaging (Fig. 3e). The mice were subcutaneously administered Cy5-labeled OVA in $MnCl_2$ solution, the GAgel, or GA@Mn. The fluorescence signals at the injection site were tracked using an *in vivo* imaging system (AniView 100). In the $MnCl_2$ group, fluorescence became nearly undetectable by day 3. The GAgel group showed fading signals from day 3 onward, with complete loss by day 10. In contrast, GA@Mn maintained detectable fluorescence for up to 14 days (Fig. 3f and Fig. S9), indicating significantly prolonged antigen retention attributable to enhanced depot formation. Sustained Mn^{2+} retention is equally critical for prolonged local immunostimulation and minimizing systemic exposure. We quantitatively assessed Mn^{2+} levels at the injection site and in the major organs using ICP-MS. In the $MnCl_2$ group, Mn^{2+} was nearly undetectable locally after 3 days. In contrast, GA@Mn maintained significant Mn^{2+} levels at the site for 14 days (Fig. 3g), confirming that coordination with GA facilitates gradual Mn^{2+} release. Uncontrolled systemic diffusion of metal ions can lead to accumulation in various organs, particularly the liver and kidneys, which poses toxicity risks and hinders clinical translation.[32–34] In this study, Mn^{2+} levels in the major organs were quantified at days 0, 0.5, 1, 3, 7, and 14 post-injection. On day 0.5, the $MnCl_2$ group exhibited approximately two-fold higher hepatic and renal Mn^{2+} levels than the GA@Mn group; these levels returned to the baseline by day 14. In the GA@Mn-treated mice, the organ-level Mn^{2+} remained consistently lower throughout the study (Fig. 3g and Fig. S10a–c), indicating controlled release that avoids systemic spikes and improves local bioavailability. Furthermore, we collected serum from the mice injected with $MnCl_2$ or GA@Mn at different time points post-injection to measure the Mn^{2+} concentration in the blood and changes in key biochemical indicators, aiming to assess potential bodily damage caused by the metabolism of the metal ion Mn^{2+}. The change in serum Mn^{2+} levels (Fig. S11) showed that the mice injected with the $MnCl_2$ solution experienced a rapid initial increase in the blood Mn^{2+} concentration, followed by a gradual decrease. In contrast, the peak serum Mn^{2+} concentration in the mice injected with GA@Mn was only one-third of that in the $MnCl_2$ group. The blood biochemical analysis results revealed that, compared to the mice injected with GA@Mn, the serum levels of AST, CREA, UA, and UREA were significantly higher in the $MnCl_2$-injected mice at the measured time points (Fig. S12). This indicates that the rapid diffusion of metal ions in the solution form can cause acute damage to the liver and kidneys in a short period. In summary, the enhanced mechanical properties of GA@Mn enable sustained codelivery of the antigen and Mn^{2+} at the injection site. This synchronized release supports prolonged immunostimulation while reducing systemic exposure, offering a promising strategy for effective and safe vaccine adjuvant.[35]

3.6. GA@Mn activates the cGAS-STING pathway, promoting DC maturation and antigen uptake

Mn^{2+} is known to activate the cGAS-STING pathway and promote immune cell maturation upon innate immune activation (Fig. 4a).[36] The application of cGAS-STING agonists, especially Mn^{2+}, as vaccine adjuvants to bridge innate and adaptive immunity represents a promising research direction.[37] To evaluate whether GA@Mn activates APCs *via* the cGAS–STING pathway, DC2.4 cells were treated with GAgel leachates, GA@Mn leachates, or $MnCl_2$ solution. WB analysis showed that GA@Mn significantly increased the levels of p-STING and p-IRF3 compared to controls (Fig. 4b and Fig. S13a and b), confirming that GA@Mn preserves the bioactivity of Mn^{2+} and induces phosphorylation of key proteins in the STING pathway. Activated STING promotes the nuclear production of TANK-binding kinase 1 (TBK1) (Fig. 4b and Fig. S13c), which can subsequently activate nuclear factor-κB (NF-κB) and stimulate type I interferon (IFN) secretion, thereby initiating innate immune responses. DC maturation serves as a critical link between innate and adaptive immunity. Mature DCs (mDCs) upregulate co-stimulatory molecules such as CD80 and CD86, which are essential for antigen uptake and presentation.[38] BMDCs were incubated with GA@Mn or control materials, and maturation was assessed *via* flow cytometry. Consistent with earlier reports, Mn^{2+} alone markedly enhanced the expression of CD80 and CD86, while GA@Mn induced similar levels of both markers among all groups (Fig. 4c). Antigen uptake was evaluated by incubating BMDCs with FITC-OVA-loaded formulations. CLSM revealed stronger intracellular fluorescence in the $MnCl_2$ and GA@Mn groups (Fig. 4d), indicating enhanced antigen internalization, which is a crucial step for subsequent antigen processing and presentation. We further evaluated the activation of cGAS-STING pathway activation by GA@Mn *in vivo*. The mice were subcutaneously injected with 200 μL of PBS, VLPs, $MnCl_2$, the GAgel, or GA@Mn, respectively. Tissues from the injection site were collected 24 h post-injection, and the expression of key cytokines related to the cGAS–STING pathway was analyzed using RT-qPCR. Both $MnCl_2$ and GA@Mn significantly upregulated the transcription of IRF3, NF-κB, and TBK1 (Fig. S14), confirming activation of the STING pathway. Moreover, GA@Mn

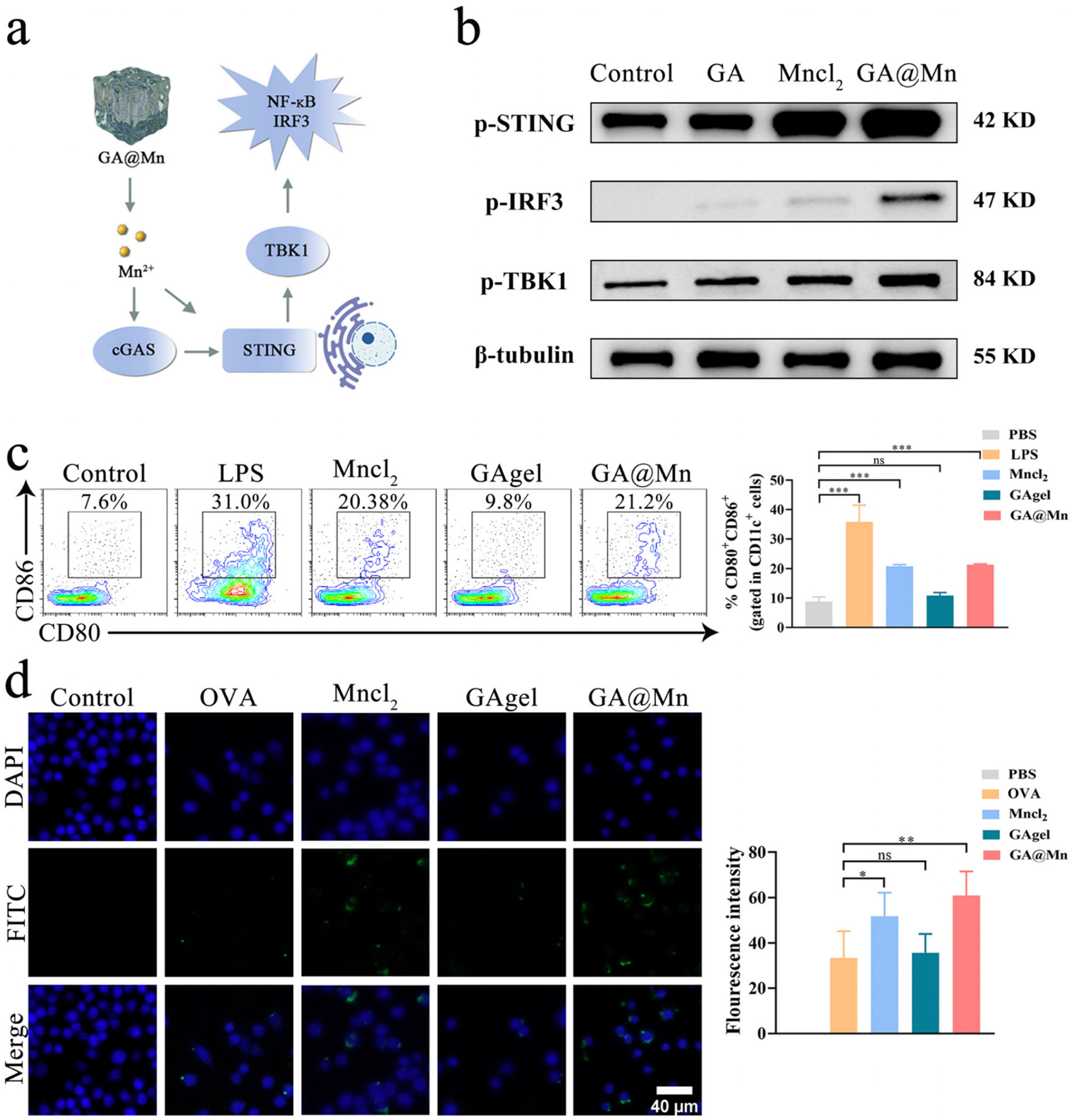

Fig. 4 GA@Mn activates the cGAS–STING pathway, promoting DC maturation and antigen uptake. (a) Schematic illustration of Mn^{2+}-mediated cGAS–STING activation. (b) WB analysis of the phosphorylation levels of cGAS–STING-related signaling proteins in DC2.4. (c) Flow cytometry analysis of $CD80^+CD86^+$ DC11c cells. (d) CLSM analysis of FITC-OVA uptake by DCs. Scale bar: 40 μm.

induced higher expression of TNF-α and IL-6 compared to the GAgel (Fig. S15), consistent with pro-inflammatory cytokine production driven by cGAS–STING activation.

3.7. GA@Mn promotes APC recruitment and establishes a favorable immune microenvironment

In addition to detecting STING pathway activation, we examined chemokine expression at the injection site of mice *via* RT-qPCR. The GA@Mn hydrogel significantly upregulated the expression of CCL-2, CCL-3, CXCL-2, and CXCL-5 (Fig. 5a), suggesting its potential to promote immune cell recruitment.[39] To further evaluate immune cell recruitment, the mice were subcutaneously injected with 200 μL of the GAgel or GA@Mn. Five days post-injection, the hydrogels were excised for histological analysis and cellular quantification, while infiltrating immune subsets were characterized by flow cytometry. Macroscopically, GA@Mn elicited pronounced cellular infiltration with the formation of distinct nodules (Fig. S16). H&E staining revealed that immune cells in the GAgel were largely restricted to the periphery of the scaffold, whereas GA@Mn supported extensive and uniform infiltration throughout the hydrogel matrix (Fig. 5b), demonstrating its superior capacity

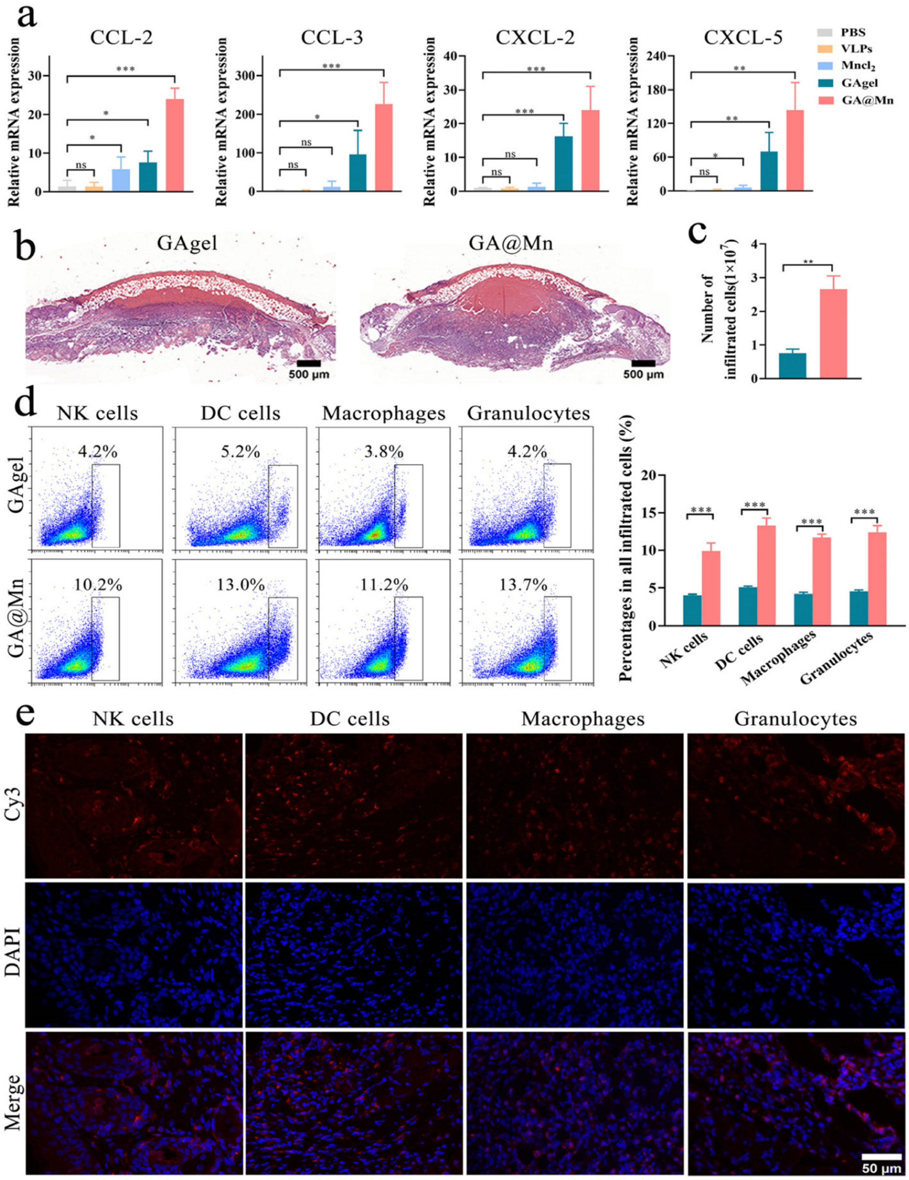

Fig. 5 GA@Mn promotes immune cell recruitment and facilitates a favorable immune microenvironment. (a) RT-PCR analysis of mRNA levels of CCL-2, CCL-3, CXCL-2, and CXCL-5 at the injection site of mice across treatment groups. (b) H&E staining of cell recruitment in the GAgel and GA@Mn. (c) Quantification of total recruited cells in the GAgel and GA@Mn. (d) Flow cytometry analysis of the percentages of NK cells, DCs, macrophages and granulocytes among recruited cells in the GAgel and GA@Mn. (e) Spatial distribution of NK cells, DC cells, macrophages and granulocytes (red) in the GA@Mn hydrogel. Nuclei were counterstained with DAPI (blue). Scale bar: 50 μm.

for immune cell recruitment and penetration. Quantitative analysis confirmed a significantly higher number of recruited cells in GA@Mn compared to the GAgel (Fig. 5c). Flow cytometry further indicated that immune cells accounted for up to 40% of the total cells recruited by GA@Mn, including DCs (13.0%), macrophages (11.2%), granulocytes (13.7%), and NK cells (10.2%) (Fig. 5d). Notably, APCs constituted the predominant population among the recruited cells, forming an immune-favorable niche conducive to the initiation and amplification of adaptive immunity. To spatially resolve the immune microenvironment constructed by the GA@Mn hydrogel, we performed immunofluorescence staining on sections from the injection site. Consistent with the widespread cellular infiltration indicated by H&E staining, fluorescence imaging visually revealed the distribution characteristics of recruited immune cells within the GA@Mn hydrogel matrix. The immunofluorescence imaging results showed that NK cells, DCs, macrophages, and granulocytes exhibited a uniform, diffuse distribution throughout the internal scaffold of the hydrogel (Fig. 5e). This spatial distribution pattern further indicates that the GA@Mn hydrogel can effectively recruit various immune cells to the injection site, creating an immune microenvironment conducive to antigen processing and presentation.

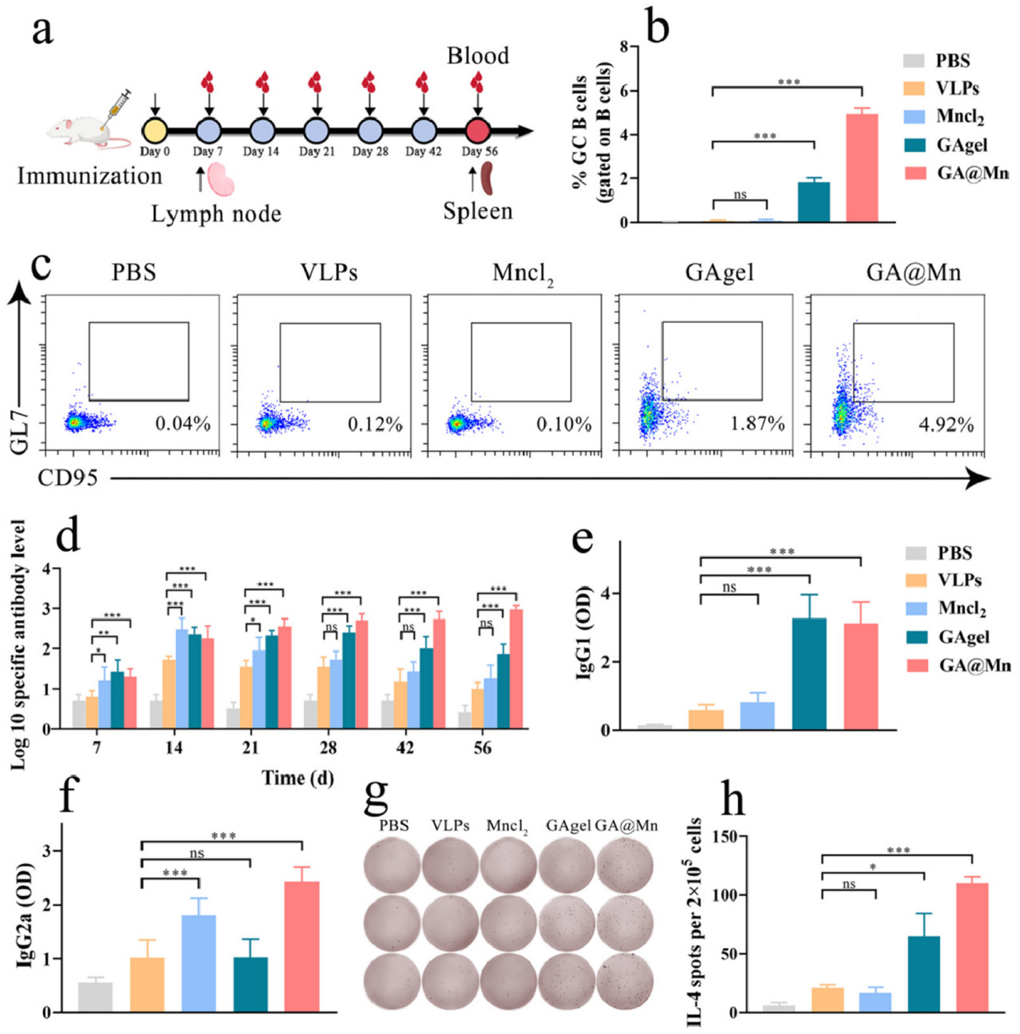

Fig. 6 GA@Mn promotes GC formation and elicits potent humoral immunity. (a) Schematic of immunization and serum collection schedule. (b and c) Flow cytometry analysis of GC B cells in lymph nodes at one week post-injection. (d) ELISA of antigen-specific IgG titers in serum. (e and f) Indirect ELISA of IgG1 and IgG2a levels in serum. (g and h) ELISpot analysis of IL-4-secreting splenocytes after antigen restimulation.

3.8. GA@Mn promotes GC formation and induces potent humoral immunity

Having established that GA@Mn activates innate immunity and recruits immune cells *in vivo* to establish an immunologically favorable microenvironment, we next evaluated its capacity to induce antigen-specific adaptive immune responses in the mice. FMD VLPs were employed as the antigen to prepare GAgel and GA@Mn hydrogel vaccines. Solution-based vaccines were formulated by dispersing FMD VLPs in PBS or $MnCl_2$ solution. The mice received a single immunization dose (Fig. 6a), and both humoral and cellular immune responses were assessed. GC reactions play a pivotal role in humoral immunity by facilitating the positive selection and clonal expansion of B cells, leading to high-affinity antibody production.[40] The expression of transcription factors Bcl6 and Bach2 is closely linked to GC formation and serves as a key indicator of GC activation. On day 7 post-immunization, RNA extracted from lymph node cells of the immunized mice was analyzed *via* RT-qPCR. GA@Mn significantly upregulated Bcl6 and Bach2 expression compared to FMD VLPs alone (Fig. S17), indicating robust GC activation. Flow cytometric analysis of lymph nodes further revealed that the GA@Mn group had a markedly higher proportion of GC B cells, which was 2.6-fold greater than that in the GAgel group (Fig. 6b and c), likely attributable to its enhanced antigen depot effect.

The serum samples collected at designated time points were evaluated for antigen-specific IgG titers. At day 14, the $MnCl_2$-formulated VLP solution vaccine induced the highest IgG titers, though these levels declined rapidly thereafter. The GAgel elicited lower and transient antibody responses, likely due to the absence of Mn^{2+} adjuvant and its limited mechanical stability. In contrast, GA@Mn produced gradually increasing, high-level, and sustained antigen-specific antibody titers (Fig. 6d), demonstrating that its hydrogel scaffold enhances both the magnitude and durability of humoral immunity through sustained release of the antigen and Mn^{2+}.

To further characterize the humoral response, we profiled IgG subclasses, which reflect distinct immune polarizations. VLPs alone primarily induced a Th2-biased IgG1 response, while the addition of Mn^{2+} increased IgG2a levels. The GAgel similarly elicited an IgG1-dominated profile (Fig. 6e and f). Notably, GA@Mn generated the highest levels of both IgG1 and IgG2a, suggesting a mixed Th1/Th2 humoral immune phenotype. On day 56, ELISpot analysis revealed that the GAgel increased the number of antigen-specific IL-4-secreting cells by 3.1-fold compared to VLPs alone, whereas GA@Mn induced a 5.2-fold increase (Fig. 6g and h), further corroborating that Mn^{2+} coordination enhances the hydrogel's antigen depot functionality and amplifies humoral immunity.

To further evaluate the ability of GA@Mn to enhance vaccine immunogenicity, we analyzed the neutralizing antibody levels in serum on day 28 post-immunization. Compared to the $MnCl_2$ solution and the GAgel hydrogel, GA@Mn maximally increased the neutralizing antibody levels, achieving a neutralizing antibody titer of 2.3 Log_{10} (Fig. S18). Based on the correlation we previously established,[41] it can be estimated that GA@Mn formulated with FMD VLPs can provide approximately 84% protection against challenge at 28 days post-immunization. To assess the broad applicability of GA@Mn, we further immunized the mice with the model antigen OVA. On day 28 post-immunization, the GAgel hydrogel and $MnCl_2$ solution moderately increased the levels of OVA-specific antibodies and their IgG1 and IgG2a subtypes to varying degrees (Fig. S19). GA@Mn demonstrated the highest capability in enhancing specific antibody and subtype levels, indicating that the GA@Mn vaccine delivery system is also applicable to the model antigen OVA.

3.9. GA@Mn amplifies cellular immunity and immunological memory

Mn^{2+} activates the STING pathway, stimulates IFN-γ production, and plays a pivotal role in cellular immune activation.[42] To evaluate the cellular immune response induced by GA@Mn, splenic lymphocytes were isolated from the immunized mice on day 28 post-immunization, and the antigen-specific cytotoxic T lymphocyte (CTL) activity was assessed *via* the GzmB level (Fig. 7a). The GA@Mn group exhibited the highest GzmB concentration, exceeding that of the VLP, $MnCl_2$, and GAgel groups by 6.6-fold, 1.2-fold, and 6.5-fold, respectively (Fig. 7b), indicating a substantially enhanced antigen-specific T cell response. The frequency of antigen-specific IFN-γ-producing cells was further evaluated using ELISpot. Consistent with the CTL results, GA@Mn immunization induced a markedly higher number of IFN-γ-secreting cells compared to all other groups (Fig. 7c and d), confirming that Mn^{2+} coordination enhances the hydrogel's ability to promote cellular immunity. Immune memory is critical for rapid and potent responses upon pathogen re-exposure. TEM and TCM contribute to long-term immunity by mediating swift and robust recall responses.[43] On day 56 post-immunization,

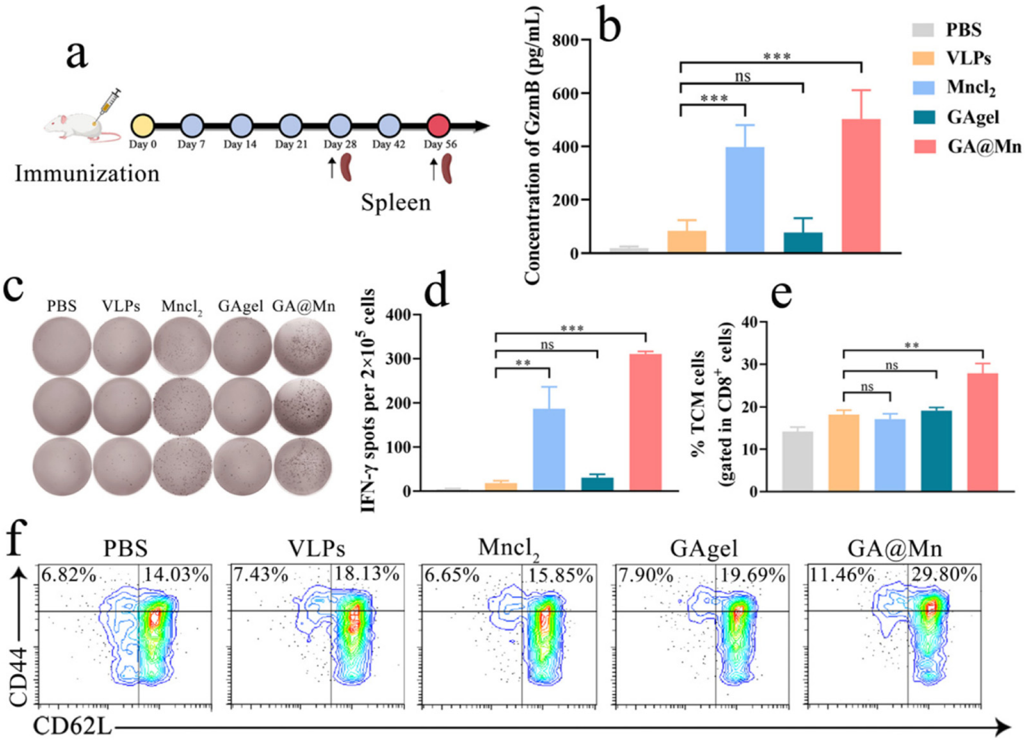

Fig. 7 GA@Mn promotes cellular immunity. (a) Schematic of immunization and sample collection schedule. (b) ELISA of GzmB levels across treatment groups. (c and d) ELISpot analysis of IFN-γ-secreting splenocytes after antigen restimulation. (e and f) Flow cytometry of TCM percentages among splenic $CD8^+$ T cells.

splenic memory T cell subsets were analyzed by flow cytometry. GA@Mn immunization significantly increased the proportions of both TEM and TCM compared to all other treatments (Fig. 7e, f and Fig. S20), demonstrating its capacity to establish durable immune memory. These results indicate that GA@Mn not only enhances effector T cell responses but also facilitates the generation of long-lived memory T cell subsets. This effect is likely due to the sustained release of the antigen and Mn^{2+} from the hydrogel, which provides prolonged immunostimulation and supports the development of lasting immune memory.

3.10. Excellent *in vivo* biocompatibility of GA@Mn

The *in vivo* biocompatibility of GA@Mn is critical for its further development and potential clinical translation. To evaluate its safety profile, blood samples and the major organs (heart, liver, spleen, kidneys, and lungs) were collected from the mice 56 days after immunization. Comprehensive assessments were conducted through hematological analysis, serum biochemistry, and histopathological examination. All hematological parameters, including HGB, MCH, MCHC, MCV, RBC, and WBC, remained within normal physiological ranges across all experimental groups (Fig. S21a). Similarly, serum biochemical markers such as ALB, ALT, AST, CREA, UA, and UREA also fell within normal reference values in all treatments (Fig. S21a). Histological evaluation further confirmed the absence of pathological changes or structural abnormalities in the major organs of GA@Mn-treated mice compared to controls (Fig. S21b). Together, these results demonstrate that GA@Mn does not induce detectable toxicity or adverse effects in the major organ systems, hematopoiesis, or liver function, underscoring its excellent biocompatibility and strong potential for clinical application.

4. Conclusions

In this study, we engineered a GA@Mn hydrogel-based vaccine delivery platform through coordination-driven self-assembly of GA and Mn^{2+}. The incorporation of Mn^{2+} not only facilitated GA supramolecular organization but also significantly enhanced the mechanical robustness of the resulting hydrogel, effectively addressing the limited structural stability typical of small-molecular hydrogels and substantially prolonging antigen persistence at the injection site. Crucially, Mn^{2+} was stably integrated into the nanofiber network not merely by physical encapsulation but *via* coordination binding. This approach enabled a sustained release of Mn^{2+} that was synchronized with hydrogel degradation, ensuring prolonged immunostimulation. Meanwhile, this platform facilitated substantial recruitment of immune cells and the establishment of a favorable microenvironment conducive to antigen presentation. Moreover, GA@Mn activated the cGAS–STING pathway, enhanced DC maturation and antigen uptake, and ultimately provoked robust antigen-specific humoral and cellular immune responses following a single administration.

By synergizing the Th1-biased immunity driven by Mn^{2+} with the depot-based Th2-polarization capability of the hydrogel, GA@Mn represents a well-defined, mechanistically elucidated, and highly potent vaccine delivery system with significant promise for clinical translation.

Author contributions

Jingjing Zhou: investigation, methodology, formal analysis, validation, writing – original draft, and funding acquisition. Shengying Zhang: methodology, formal analysis, and validation. Hu Dong: methodology and formal analysis. Yunhua Li: methodology. Haoyue Zang: methodology and validation. Zhidong Teng: methodology. Mingyang Zhang: methodology. Yifan Liu: methodology. Shiqi Sun: investigation, funding acquisition, and writing – review & editing. Huichen Guo: conceptualization, funding acquisition, and writing – review & editing.

Conflicts of interest

There are no conflicts to declare.

Data availability

All data supporting the findings of this study are available within the article and its supplementary information (SI). Supplementary information is available. See DOI: https://doi.org/10.1039/d5nr04283f.

Acknowledgements

This work was supported by grants from the National Natural Science Foundation of China (No. 32301127 and 32473012), the Natural Science Foundation of Gansu Province (No. 25JRRA442 and 25JRRA1089) and the Gansu Longyuan Youth Innovation and Entrepreneurship Talent Program-Youth Team (No. 2025QNTD34).

References

1 Y. Sheng, Z. Li, X. Lin, L. Wang, H. Zhu, Z. Su and S. Zhang, *J. Controlled Release*, 2024, **368**, 275–289.
2 X. Fan, F. Liu, F. Sun, Y. Wang, W. Shen, S. Wang, J. Sun and K. Wang, *Acta Pharm. Sin. B*, 2025, **9**, 4644–4672.
3 R. Guyon, S. Reinke, A. Truby, L. Sims, A. V. S. Hill, L. Bau, E. Stride and A. Milicic, *Sci. Transl. Med.*, 2025, **17**, eadw2256.
4 H. Jia, J. Lin, D. Wang, X. Lv, Q. Wang, Z. Wang, J. Liu, L. Yang and J. Liu, *Adv. Funct. Mater.*, 2024, **34**, 2315442.

5 P. Wang, Y. Wang, H. Li, M. Wang, Y. Wang, X. Wang, L. Ran, H. Xin, J. Ma, G. Tian, W. Gao and G. Zhang, *Acta Biomater.*, 2024, **177**, 400–413.

6 R. Zhang, C. Wang, Y. Guan, X. Wei, M. Sha, M. Yi, M. Jing, M. Lv, W. Guo, J. Xu, Y. Wan, X. M. Jia and Z. Jiang, *Cell. Mol. Immunol.*, 2021, **18**, 1222–1234.

7 K. M. Garland, T. L. Sheehy and J. T. Wilson, *Chem. Rev.*, 2022, **122**, 5977–6039.

8 L. Yang, Y. Wang, Y. Song, Z. Li, L. Lei, H. Li, B. He, J. Cao and H. Gao, *J. Controlled Release*, 2024, **370**, 354–366.

9 Y. Zhao, X. Zhao, X. Wang, Z. Ma, J. Yan, S. Li, N. Wang, J. Jiao, J. Cui and G. Zhang, *Acta Biomater.*, 2025, **193**, 417–428.

10 M. E. Aikins, X. Sun, H. Dobson, X. Zhou, Y. Xu, Y. L. Lei and J. J. Moon, *J. Controlled Release*, 2024, **368**, 768–779.

11 H. Hao, S. Wu, J. Lin, Z. Zheng, Y. Zhou, Y. Zhang, Q. Guo, F. Tian, M. Zhao, Y. Chen, X. Xu, L. Hou, X. Wang and R. Tang, *Nat. Biomed. Eng.*, 2023, **7**, 928–942.

12 X. Dong, P. Pan, Q. Zhang, J. J. Ye and X. Z. Zhang, Engineered living bacteriophage-enabled self-adjuvanting hydrogel for remodeling tumor microenvironment and cancer therapy, *Nano Lett.*, 2023, **23**, 1219–1228.

13 V. H. Giang Phan, H. T. T. Duong, T. Thambi, T. L. Nguyen, M. H. Turabee, Y. Yin, S. H. Kim, J. Kim, J. H. Jeong and D. S. Lee, *Biomaterials*, 2019, **195**, 100–110.

14 X. X. Li, Y. Z. Wang, S. W. Wang, C. H. Liang, G. J. Pu, Y. X. Chen, L. Wang, H. Xu, Y. Shi and Z. Zhang, *Nanoscale*, 2020, **12**, 2111–2117.

15 Z. Y. Wang, C. H. Liang, F. Shi, T. He, C. Y. Gong, L. Wang and Z. Zhang, *Nanoscale*, 2017, **9**, 14058–14064.

16 C. Korupalli, W. Y. Pan, C. Y. Yeh, P. M. Chen, F. L. Mi, H. W. Tsai, Y. Chang, H. J. Wei and H. W. Sung, *Biomaterials*, 2019, **216**, 119268.

17 C. Zhang, E. Cai, X. Qi, X. Ge, Y. Xiang, J. Wang, Y. Li, L. Lv, H. Zheng, Y. Qian, W. Dong, H. Li and J. Shen, *Chem. Eng. J.*, 2024, **487**, 150756.

18 W. Luo, Z. Yang, J. Zheng, Z. Cai, X. Li, J. Liu, X. Guo, M. Luo, X. Fan, M. Cheng, T. Tang, J. Liu and Y. Wang, Small molecule hydrogels loading small molecule drugs from chinese medicine for the enhanced treatment of traumatic brain injury, *ACS Nano*, 2024, **18**, 28894–28909.

19 K. Chen, X. Wu, Q. Wang, Y. Wang, H. Zhang, S. Zhao, C. Li, Z. Hu, Z. Yang and L. Li, *Chem. Lett.*, 2023, **34**, 107446.

20 Y. Qian, Y. Zheng, J. Jin, X. Wu, K. Xu, M. Dai, Q. Niu, H. Zheng, X. He and J. Shen, *Adv. Mater.*, 2022, **34**, e2200521.

21 W. Liu, Z. Li, Z. Wang, Z. Huang, C. Sun, S. Liu, Y. Jiang and H. Yang, *ACS Appl. Mater. Interfaces*, 2023, **15**, 7767–7776.

22 X. Yu, J. Cai, M. Xu, Q. Li, Y. Yang, Z. Wan and X. Yang, *Nanoscale*, 2024, **16**, 14261–14268.

23 W. Xu, Z. Lin, C. J. Kim, Z. Wang, T. Wang, C. Cortez-Jugo and F. Caruso, *Sci. Adv.*, 2024, **10**, eads9542.

24 T. Guan, Z. Chen, X. Wang, S. Gao, X. Lu, Y. Li, Z. Wang, S. Zhang, Y. Guo, M. Guo, Y. Cui, Y. Wang and C. Chen, *J. Am. Chem. Soc.*, 2025, **147**, 6523–6535.

25 H. Guo, S. Sun, Y. Jin, S. Yang, Y. Wei, D. Sun, S. Yin, J. Ma, Z. Liu, J. Guo, J. Luo, H. Yin, X. Liu and D. Liu, *Vet. Res.*, 2013, **44**, 1–13.

26 X. Zhao, H. Zhang, Y. Gao, Y. Lin and J. Hu, *ACS Appl. Bio Mater.*, 2020, **3**, 648–653.

27 J. Hao, Y. Gao, J. Liu, J. Hu and Y. Ju, *ACS Appl. Mater. Interfaces*, 2020, **12**, 4927–4933.

28 X. Yu, M. Xu, J. Cai, Q. Li, Y. Yang, Z. Wan and X. Yang, *Giant*, 2024, **17**, 100240.

29 E. Su, Q. Li, M. Xu, Y. Yuan, Z. Wan, X. Yang and B. P. Binks, *J. Colloid Interface Sci.*, 2020, **11**, 797–809.

30 Y. Qian, Y. Zheng, J. Jin, X. Wu, K. Xu, M. Dai, Q. Niu, H. Zheng, X. He and J. Shen, *Adv. Mater.*, 2022, **2200521**, 1–15.

31 H. Song, Q. Su, Y. Nie, C. Zhang, P. Huang, S. Shi, Q. Liu and W. Wang, *Acta Biomater.*, 2023, **158**, 535–546.

32 X. Sun, X. Zhou, X. Shi, O. A. Abed, X. An, Y. L. Lei and J. J. Moon, *Nat. Biomed. Eng.*, 2024, **8**, 1073–1091.

33 X. Liu, Y. Liu, X. Yang, X. Lu, X. N. Xu, J. Zhang and R. Chen, *ACS Appl. Mater. Interfaces*, 2023, **15**, 48871–48881.

34 J. H. Lee, H. J. Sutton, C. A. Cottrell, I. Phung, G. Ozorowski, L. M. Sewall, R. Nedellec, C. Nakao, M. Silva, S. T. Richey, J. L. Torres, W. H. Lee, E. Georgeson, M. Kubitz, S. Hodges, T. M. Mullen, Y. Adachi, K. M. Cirelli, A. Kaur, C. Allers, M. Fahlberg, B. F. Grasperge, J. P. Dufour, F. Schiro, P. P. Aye, O. Kalyuzhniy, A. Liguori, D. G. Carnathan, G. Silvestri, X. Shen, D. C. Montefiori, R. S. Veazey, A. B. Ward, L. Hangartner, D. R. Burton, D. J. Irvine, W. R. Schief and S. Crotty, *Nature*, 2022, **609**, 998–1004.

35 B. S. Ou, O. M. Saouaf, J. Yan, T. U. J. Bruun, J. Baillet, X. Zhou, N. P. King and E. A. Appel, *Adv. Healthcare Mater.*, 2023, **12**, e2301495.

36 X. Zhang, X. C. Bai and Z. J. Chen, *Immunity*, 2020, **53**, 43–53.

37 Q. R. Li, X. Zhang, C. Zhang, Y. Zhang, M. T. Niu, Z. Chen, S. M. Zhang, J. He, W. H. Chen and X. Z. Zhang, *J. Am. Chem. Soc.*, 2025, **147**, 24555–24572.

38 S. H. Zhou, R. Y. Zhang, Z. W. You, Y. K. Zou, Y. Wen, J. Wang, D. Ding, M. M. Bian, Z. M. Zhang, H. Yuan, G. F. Yang and J. Guo, *ACS Appl. Mater. Interfaces*, 2023, **15**, 8914–8926.

39 W. Fu, M. Guo, X. Zhou, Z. Wang, J. Sun, Y. An, T. Guan, M. Hu, J. Li, Z. Chen, J. Ye, X. Gao, G. F. Gao, L. Dai, Y. Wang and C. Chen, *ACS Nano*, 2024, **18**, 11200–11216.

40 J. Deng, Z. Wang, L. Wu, Z. Song, H. S. Bahlol, X. Li, L. Zhao and H. Han, *ACS Nano*, 2025, **19**, 9042–9052.

41 H. Li, A. Dekker, Y. Zhang, Y. Zhang, M. Harmsen, W. Poel, H. Guo and S. Sun, *Vaccine*, 2025, **62**, 1–5.

42 C. Dong, Y. Wang, W. Zhu, Y. Ma, J. Kim, L. Wei, G. X. Gonzalez and B. Z. Wang, *ACS Appl. Mater. Interfaces*, 2022, **14**, 6331–6342.

43 X. Deng, T. Liu, Y. Zhu, J. Chen, Z. Song, Z. Shi and H. Chen, *Bioact. Mater.*, 2024, **33**, 483–496.